Journal of Materials Chemistry A

Guidelines for designing high-deformability materials for all-solid-state lithium-ion batteries

Journal:	*Journal of Materials Chemistry A*
Manuscript ID	TA-COM-04-2024-002328.R1
Article Type:	Communication
Date Submitted by the Author:	07-Jun-2024
Complete List of Authors:	Tanibata, Naoto; Nagoya Institute of Technology, Advanced Ceramics Aizu, Shin; Nagoya Institute of Technology, Advanced Ceramics Koga, Misato; Nagoya Institute of Technology Takeda, Hayami; Nagoya Institute of Technology Creative Engineering Program, Kobayashi, Ryo; Nagoya Institute of Technology, Physical Science and Engineering Nakayama, Masanobu; Nagoya Institute of Technology, Department of Materials Science and Engineering

ARTICLE

Guidelines for designing high-deformability materials for all-solid-state lithium-ion batteries†

Received 00th January 20xx,
Accepted 00th January 20xx

DOI: 10.1039/x0xx00000x

Naoto Tanibata,*[a] Shin Aizu,[a] Misato Koga,[a] Hayami Takeda,[a] Ryo Kobayashi [b] and Masanobu Nakayama[a]

Weak contact and high resistance between ceramic powder particles limit their applicability in all-solid-state Li-ion batteries, particularly those assembled via powder moulding. To overcome these limitations, sulfide and chloride materials have been extensively studied because their deformability and Li diffusivity are typically greater than those of oxide materials. However, not all sulfide and chloride materials exhibit the high Li diffusivity and deformability necessary for all-solid-state batteries. This study focused on determining the suitability of the shear modulus as an index of deformability, in addition to a Li diffusivity index. These indices were calculated for all the Li-containing chloride compounds in a structural database. Six chloride materials (Li_2CoCl_4, Li_2CrCl_4, $Li_{10}Mg_7Cl_{24}$, $Li_4Mn_3Cl_{10}$, Li_2FeCl_4, and $LiAlCl_4$) with different shear moduli were experimentally evaluated. The Li diffusion coefficients of most of these chlorides were found to be higher than those of the oxide and sulfide electrode materials typically employed in Li-ion batteries. Moreover, deformability, which for compressed pellets includes contributions from the relative density and grain boundary resistance, was observed to vary among these chlorides. The shear modulus, as determined by first-principles calculations, was confirmed to be a suitable screening index for deformability. The utilisation of the design guidelines for deformability is expected to facilitate significant advancements in all-solid-state battery material research.

Introduction

Energy-storage batteries can help address energy and environmental challenges.[1] All-solid-state lithium-ion batteries are promising next-generation batteries because they offer a combination of safety, high energy density, and high rate performance.[2–4] The use of solid electrolytes instead of conventional liquid electrolytes can reduce the risk of leakage and ignition in these batteries[5]. In addition, high energy density can be achieved using electrode materials (e.g. sulfur [6–8] and chloride electrodes [9,10]) that can be leached into liquid electrolytes. Moreover, a dense electrolyte layer can suppress short circuits due to dendrite deposition, which is a problem in lithium metal electrodes with an ultimate energy density.[11,12] However, weak contact between the particles and large interfacial resistance are major issues limiting the applicability of solid electrolytes.[13–17] In general, contact between oxide material particles is established during sintering.[18,19] However, high-temperature sintering processes may lead to the volatilisation of lithium elements[20,21] and result in side reactions between different materials (e.g. electrode–electrolyte reactions), which limits the selection of materials and processes.[22,23]

Sulfide and chloride materials,[8,24–27] which contain highly polarisable anions, have been widely studied because some of them can be densified simply via powder compression. However, not all sulfide and chloride materials exhibit high deformability in addition to high Li diffusivity, which are both important physical properties for the materials used in all-solid-state batteries.[28] Computational approaches are one of the solutions used to identify compounds that satisfy the requirements for Li^+ conductivity and deformability. High-throughput computational approaches have been extensively utilised to reveal novel Li^+ ionic conductors with high Li^+ conductivity.[29–31] Similarly, material design guidelines for deformability can facilitate the search for effective all-solid-state battery materials. The bulk and Young's moduli are commonly used indicators of deformability.[32–35] However, to the best of our knowledge, the correlation between calculated screening values (such as these moduli) and deformability, which should facilitate the discovery of materials with high deformability, has not been reported.

Plastic deformation occurs during the fabrication of all-solid-state batteries. The stress required for this type of deformation, i.e. dislocation migration, is known as the Peierls stress (τ_p) and can be expressed using the Taylor model as follows:[36]

$$\tau_p = \frac{Gb}{2\pi s}. \quad (1)$$

[a.] Department of Advanced Ceramics, Nagoya Institute of Technology, Gokiso, Showa, Nagoya, Aichi 466-8555, Japan.
[b.] Department of Applied Physics, Nagoya Institute of Technology, Gokiso, Showa, Nagoya, Aichi 466-8555, Japan.
[c.] *Corresponding author. Email: tanibata.naoto@nitech.ac.jp
[d.] †Electronic Supplementary Information (ESI) available: Figures S1–S8, Tables S1–S4, and a supplementary note on Li diffusivity evaluation via molecular dynamics (MD) simulations. See DOI: 10.1039/x0xx00000x

Here, the spacing *s* between the slip planes and Burgers vector *b*, corresponding to the direction and distance of dislocation migration, respectively, are the parameters that define the dislocation structure. Calculating the *s* and *b* values requires the relevant dislocation structure to be reproduced. In contrast, the shear modulus *G* can be obtained from the crystal structure through first-principles calculations.[37] Fig. 1 shows the average shear moduli comprehensively calculated for the Li–Cl compounds in the structural database of the Materials Project.[38] Considering the compaction of a powder sample, we hypothesise that the average value of shear modulus is related to the stress required for deformation. In this study, the inverse of the shear modulus was used as an index of deformability. The Li diffusion coefficients were calculated using molecular dynamics simulations with a force field,[39] and the phase stabilities, i.e., the energy-above-hull values, were extracted from the database (Fig. 1). These values are presented in Table S1 (Electronic Supplementary Information, ESI†). We selected six chloride compounds with various calculated shear moduli, i.e., Li_2CoCl_4, Li_2CrCl_4, $Li_{10}Mg_7Cl_{24}$, $Li_4Mn_3Cl_{10}$,[39] Li_2FeCl_4,[40] and $LiAlCl_4$.[41] These materials are considered promising for all-solid-state batteries owing to their high thermodynamic stabilities (low energy-above-hull value of <0.10 eV/atom[42] and/or high calculated Li diffusion coefficients; some of them contain 3d transition metal ions). In this study, we experimentally evaluated the deformability (relative density and grain boundary resistance) of these materials and analysed the correlation between the calculated shear moduli and experimental deformability values.

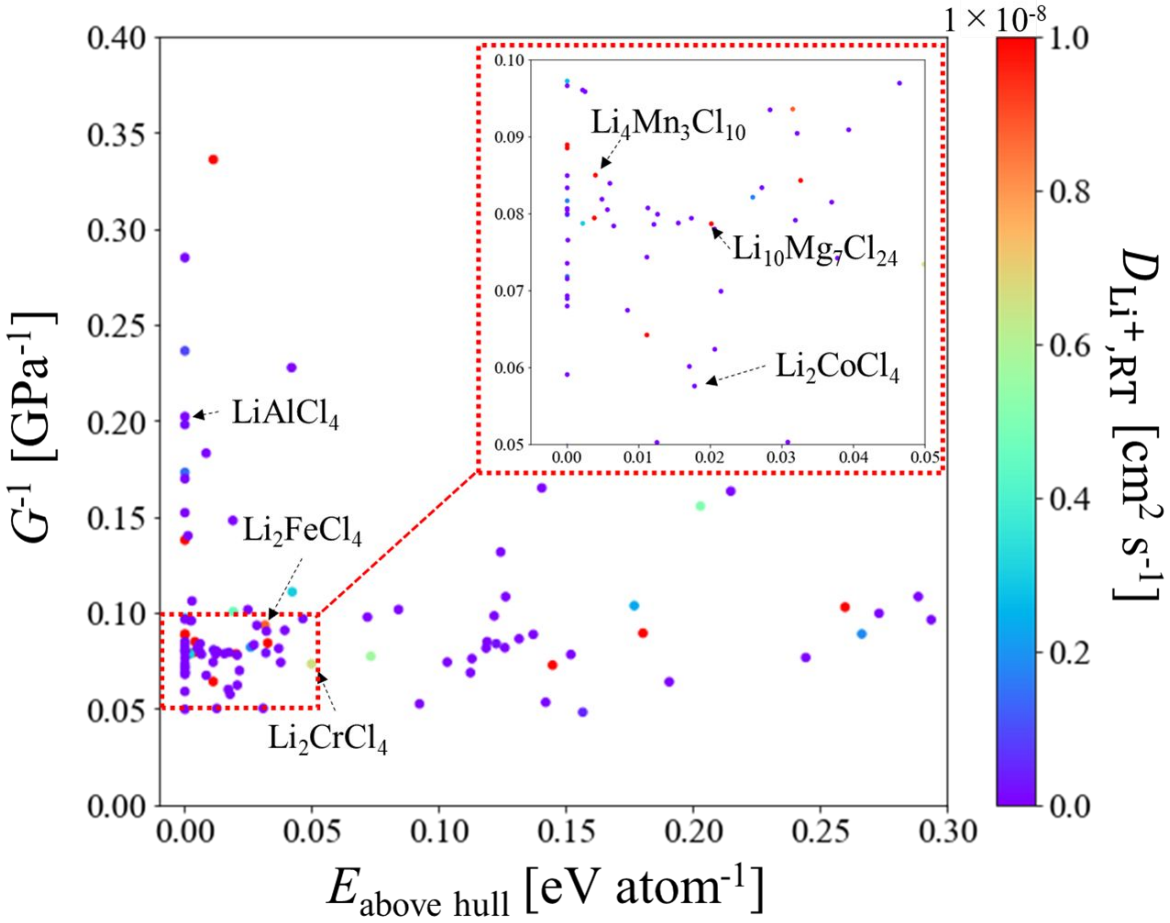

Fig. 1 Relationships among the calculated Li diffusion coefficients ($D_{Li+,RT}$), shear moduli (G), and energies above the hull for 122 Li–Cl-containing compounds. The Li diffusion coefficients of these 122 compounds among the 233 Li–Cl-containing compounds listed in a crystal structure database (Materials Project[38]) were calculated via molecular dynamics simulations using high-throughput force fields.[43] The shear moduli were calculated from the elastic tensor obtained from *ab initio* calculations.[44] The energies above the hull were extracted from the values listed in the Materials Project database. This study focused on the materials indicated in the overlaid text in the figure, with various shear moduli and low energies above the hull and/or a high Li diffusion coefficient and/or 3d transition metal content.

Experimental

Procedures

Li_2CoCl_4, $Li_{10}Mg_7Cl_{24}$, $Li_4Mn_3Cl_{10}$, Li_2FeCl_4, and $LiAlCl_4$ were synthesised via mechanochemical methods using LiCl (99.9%, Kishida Chemical Co., Ltd., Japan), $MgCl_2$ (99.99%; Sigma–Aldrich Co., LLC, America), $MnCl_2$ (99.99%; Kojundo Chemical Laboratory Co., Ltd., Japan), $FeCl_2$ (99.99%; Kishida Chemical Co., Ltd., Japan), and $AlCl_3$ (99.99%; Wako Chemicals, Japan). The corresponding stoichiometric mixtures were placed in a

45 mL ZrO_2 pot with 10 ZrO_2 balls having a diameter of 10 mm and ball-milled at 500 rpm for 24 h using a planetary ball mill (P-7 classic-line, Fritsch Japan K.K. LLC, Japan). Li_2CrCl_4 was synthesised by milling LiCl (99.9%, Kishida Chemical Co., Ltd., Japan) and $CrCl_2$ (99.99%, Sigma–Aldrich Co., LLC); it was subsequently vacuum-sealed in a Pyrex tube and heat-treated at 400 °C for 1 week. The obtained samples were identified via X-ray diffraction (XRD) with Cu Kα radiation using a diffractometer (MiniFlex 600, Rigaku Corp., Japan). The Li^+ diffusivity was determined via alternating-current (AC) impedance measurement. The powders were sandwiched between stainless steel and compressed at a pressure of 382 MPa to prepare the pellets (Φ10 mm). A voltage of 100 mV was applied at 25 °C using an electrochemical analyser (VSP, BioLogic, France). Distribution of relaxation time (DRT) analysis was performed using the Z-Assist software package (TOYO Co., Japan) to distinguish the grain boundary resistance from the total resistance. The individual resistance values were obtained by fixing the time constants obtained from the DRT analysis and fitting them to the experimentally obtained data using the complex nonlinear least squares method. The cross-sections of the pellets were examined via scanning electron microscopy (SEM; JSM-6360LV, JEOL, Japan). All procedures were performed in a dry Ar-filled atmosphere.

Calculations

A total of 233 Li–Cl-containing compounds listed in a crystal structure database (Materials Project)[38] were examined.[38] The Li diffusion coefficients were calculated via molecular dynamics simulations using the high-throughput force field (FF-MD) described in a previous study.[43]

Force-field parameters were determined using the metaheuristic algorithm (Cuckoo search[45] with density functional theory–molecular dynamics (DFT-MD) datasets. The DFT-MD simulations were performed at 25 °C for 50 ps (1 fs per step). The kinetic energy cutoff was 350 eV. Because of limited computational resources, 1 × 1 × 1 *k*-point sampling was performed. The energy convergence criterion was set to 10^{-3} eV.

Because the chloride compounds melt at elevated temperatures, the positions of the chloride ions were not allowed to change from those in the relaxed configurations during the FF-MD simulation at >500 K (Fig. S8, ESI†). The Li diffusion coefficients at 300 K were determined, assuming Arrhenius behaviour, from the diffusion coefficients at 500, 750, 1000, 1250, and 1500 K. In addition, the bulk and shear moduli were calculated using the elastic tensors obtained from DFT calculations.[46]

Results and Discussion

In addition to the materials reported in our previous studies ($Li_4Mn_3Cl_{10}$, Li_2FeCl_4, and $LiAlCl_4$),[38,39,44] three newly synthesised materials—$Li_{10}Mg_7Cl_{24}$, Li_2CrCl_4, and Li_2CoCl_4—were subjected to XRD. The obtained XRD patterns only contained peaks that could be assigned to the target compound (Fig. S1, ESI†). AC impedance measurements were performed for green compacts of the six chlorides, and diffusion coefficients were calculated using the total resistance R_{total} values obtained from Nyquist plots (Fig. 2(a) and Fig. S2, ESI†) and the Nernst–Einstein equation. R_{total} is considered to include the bulk resistance and the grain boundary resistance, which cannot easily be distinguished through visual observation. The diffusion coefficient values are presented in Table S2 (ESI†). The conductivity diffusion coefficient was calculated assuming a thermodynamic factor of unity in the chemical diffusion coefficient and is often underestimated in relation to the chemical diffusion coefficient.[47,48] Nevertheless, the conductivity diffusion coefficients of chloride materials are generally higher than the chemical diffusion coefficients of typical oxide and sulfide cathode materials (Fig. S4). These results confirm that the chloride materials have high Li^+ diffusivity and validate the computational screening method.

The powders and cross-sections of the pellets were examined via SEM (Fig. 2(c) and Figs. S2(c) and S3, ESI†). The relative densities of the materials were calculated using the true density values listed in the inorganic crystal structure database (ICSD). The relative densities vary considerably, even among the chlorides. For Li_2CoCl_4, the relative density (78%) is as low as that of the compact of an oxide ($Li_{0.33}La_{0.55}TiO_3$).[41]

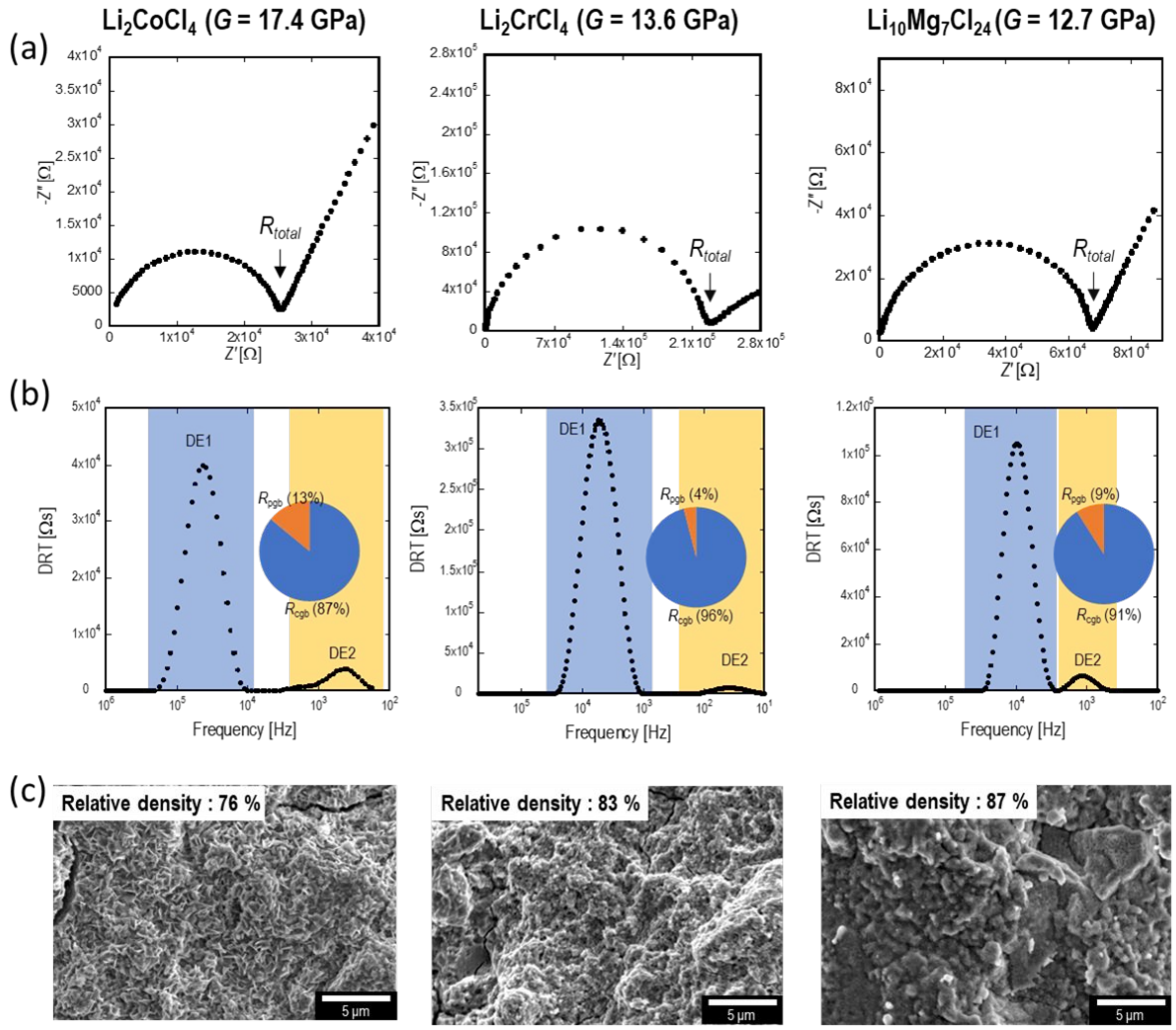

Fig. 2 Characterisation of compressed pellets of the chlorides Li_2CoCl_4, Li_2CrCl_4, and $Li_{10}Mg_7Cl_{24}$. (a) Nyquist plots. The Li diffusion coefficients were calculated from the R_{total} values using the Nernst–Einstein equation. (b) DRT spectra. The pie chart shows the relative magnitudes of the crystalline grain boundary (R_{cgb}) and particle grain boundary (R_{pgb}) resistance components calculated using DRT analysis. (c) Cross-sectional SEM images of the pellets; the relative densities are indicated.

Next, through DRT analysis,[49,50] we could distinguish the different components of the resistances obtained via AC impedance measurements (Fig. 2(b) and Fig. S2(b), ESI†). The DRT-analysis results suggest the presence of two resistance components (DE1 and DE2). Furthermore, fitting was performed using an equivalent circuit (Fig. S2(d)), where the ion-blocking electrode-derived rise is represented by CPE1. To determine the origin of each resistance component, the capacitance C was calculated from the fitted values using the following equation:[49]

$$C = \text{DE-T/DE-R}, \quad (2)$$

where DE-T and DE-R represent the relaxation time and resistance of the DE component, respectively. The obtained capacitances are presented in Table S3 (ESI†), where DE1 and DE2 have capacitances of 10^{-11}–10^{-10} and 10^{-8}–10^{-7} F, respectively. The capacitance of the crystallite bulk is known to be approximately 10^{-12} F, according to the dielectric constant values of common materials.[51] It is also known from the brickwork model that the magnitude of the capacitance of the grain boundary is proportional to the grain size; it increases, from the capacitance of the crystallite bulk, in proportion to the ratio of the grain size magnitude to the thickness of the grain boundary (~10^{-10} m)[51]. Table S3 (ESI†) also presents the crystallite size d calculated from the XRD pattern using the Halder–Wagner method[52] for each chloride along with the capacitance of the crystallite grain boundary C_{cb}, which was obtained via a brickwork model approximation (the thickness of the grain boundary was simply calculated as 10^{-10} m). The capacitance of the first resistance component is on the same order of magnitude as the capacitance of the approximated crystallite grain boundary, indicating that the origin of the first resistance component (DE1) is the crystallite grain boundary. This suggests that the resistance of the crystallite bulk may be beyond the frequency range of AC impedance measurements and hence that the ionic conductivities of the crystallite bulk are higher than the measured values. Similar considerations suggest that the capacitance of the particle grain boundary is

likely to be larger, by a factor of the ratio of the particle size to the thickness of the grain boundary, than that of the crystallite bulk. The grain boundary capacitance estimated from the particle size observed in the SEM image of the powder of each material (Fig. S3, ESI†) matches the capacitance of the second resistance component within an order of magnitude (~10^{-7} F), suggesting that the principal origin of the second resistance component (DE2) is the particle grain boundary. The ratio *Q* of the particle grain boundary resistance to the total grain boundary resistance (where the latter is defined as the sum of the crystallite grain boundary resistance and the particle grain boundary resistance) is also presented in Table S3 (ESI†) for each compound as an index of deformability.

The low particle grain boundary resistance for the Li_2CoCl_4 pellet, despite its low relative density of 76%, is probably a result of necking between the Makibishi-type particles observed in the SEM image in Fig. 2(c). The shear modulus calculation, AC impedance measurement, DRT analysis, SEM, and relative density calculation results are summarised in Fig. 3.

The correlation apparent in the figure demonstrates that the shear modulus *G* is a useful index of deformability, which is indicated by the experimentally obtained relative density values and ratio of the particle grain boundary resistance *Q*. Although these results pertain to chloride materials, the correlations among the analysed factors are expected to be applicable to oxide and sulfide materials, which are typical all-solid-state battery materials. Therefore, in this study, the same analyses (shear modulus calculation, AC impedance measurement, DRT analysis, SEM, and relative density calculation) were performed for representative oxide (Li_3BO_3, Li_2CO_3, and Li_2SO_4) and sulfide (Li_3PS_4) materials (Figs. S5 and S6 and Table S4, ESI†).[53] The AC impedance measurements for Li_3BO_3 and Li_2SO_4 were conducted at 100 °C owing to the high resistance of these compounds. A large resistive component with a capacitance of ~10^{-12} F was observed in the oxide; therefore, a fitting analysis was performed by adding DE0 as a bulk resistance to the equivalent circuit.

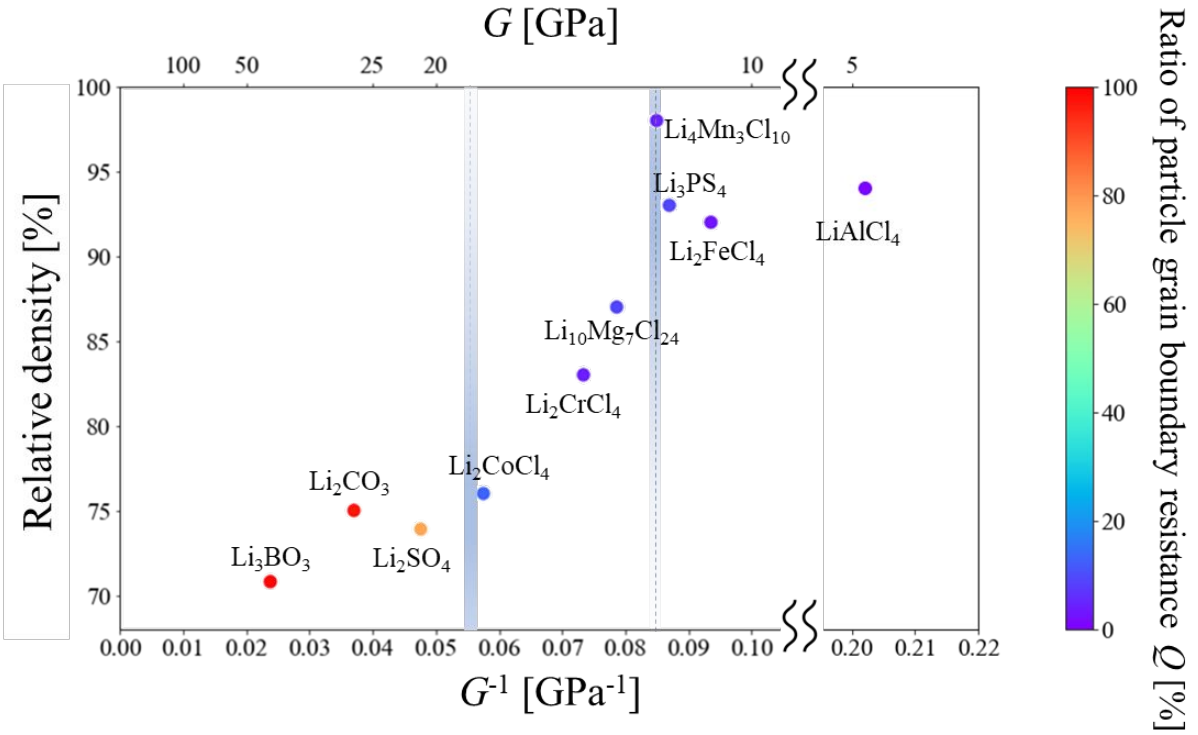

Fig. 3 Relationship between shear modulus *G* and deformability (as indicated by the experiment-derived relative density and ratio between the particle grain boundary resistance and total grain boundary resistance *Q*) for the compressed pellets of 10 materials that can be used in all-solid-state lithium-ion batteries. In addition to the data for the six chloride materials under study, those for representative oxide materials (Li_3BO_3, Li_2CO_3, and Li_2SO_4) and a sulfide material (Li_3PS_4) are shown. $LiAlCl_4$, which has a low melting point (146 °C), has a lower elastic modulus than the other compounds; therefore, the range of G^{-1} from approximately 0.11 GPa^{-1} to 0.20 GPa^{-1} is omitted.

The changes in the (i) relative density and (ii) resistance ratio of the particle grain boundary contribution as a function of the inverse shear modulus G^{-1} can be described as follows:

(i) The relative density converges at ~74%, although with some deviation due to friction with the die. This density corresponds to the densest possible structure obtained by clustering uniform rigid spheres (close-packed structure), for G^{-1} < ~0.055 GPa^{-1} (G > ~18 GPa) and increases linearly thereafter in the range of ~0.055 GPa^{-1} < G^{-1} < ~0.085 GPa^{-1}. For G^{-1} > ~0.085 GPa^{-1} (*G* < ~12 GPa), the relative density converges at ~100%.

(ii) The particle grain boundary resistance ratio *Q*, which is almost 100% in oxide compounds with high shear moduli (Li_3BO_3) (G^{-1} = 0.024 GPa^{-1}, *G* = 42.0 GPa), decreases with the shear modulus, and *Q* converges at ~10% for G^{-1} > ~0.055 GPa^{-1} (*G* < ~18 GPa).

According to these results, the following design guidelines for the deformability of all-solid-state lithium-ion battery materials are proposed:

(i) A material with a shear modulus of G < 12 GPa is preferable for obtaining ~100% density via compaction.

(ii) A material with a shear modulus of G < 18 GPa is preferable for minimising the relative magnitude of the particle grain boundary resistance (approximately 10%) via compaction.

In this study, a uniaxial pressure P of 382 MPa was used for compaction. Note, however, that these shear modulus values will vary with respect to the pressure.

By adhering to these design guidelines, according to the calculated shear modulus (G) values, the efficiency of screening for materials that exhibit the deformability required for all-solid-state batteries can be increased. Although other factors, such as particle size, particle size distribution, particle shape, crystallite size, strain, particle-tapped density, and properties related to mobile dislocation, may affect the relative density and the relative magnitude of the particle grain boundary resistance in the pellets, their impact on the results of this study is negligible. By contrast, in Fig. S7 (ESI†), the bulk modulus B[32–34] is not correlated with deformability.[32–34] This result indicates that among the different elastic moduli, the shear modulus, which is related to dislocation migration, is a suitable index of deformability. Note that even oxides and Li_2CrCl_4 with relatively low Li diffusivity follow this correlation, suggesting that the deformability indicator of shear modulus can be applied not only to battery materials but also to other fields where compacts are used.

Conclusions

We investigated the correlation between the computed shear modulus and the experimentally evaluated deformability (relative density and particle grain boundary resistance) for six chloride materials (Li_2CoCl_4, Li_2CrCl_4, $Li_{10}Mg_7Cl_{24}$, $Li_4Mn_3Cl_{10}$, Li_2FeCl_4, and $LiAlCl_4$), three oxide materials (Li_3BO_3, Li_2CO_3, and Li_2SO_4), and a sulfide material (Li_3PS_4). The deformabilities of the oxide, sulfide, and chloride materials (which were expected to be high) differed depending on the specific compound, suggesting that different compounds are suitable for different applications. The results indicated that deformability is strongly correlated with the shear modulus determined through first-principles calculations. The material design guidelines for deformability established on the basis of this strong correlation are expected to significantly increase the efficiency of the screening of materials for all-solid-state batteries. Moreover, these guidelines are expected to be extended to not only other chloride, sulfide, and oxide materials for next-generation devices but also to a wider range of materials.

Author Contributions

N. T. and M. N. conceived and designed the experiments; S. A. and H. T. performed the experiments and analysed the data; R. K. contributed materials/analysis tools; and N. T. and M. N. co-wrote the paper. All authors have approved the final version of the manuscript.

Conflicts of Interest

There are no conflicts to declare.

Acknowledgements

Computations were performed using the facilities of the Supercomputer Centre at the Institute for Solid State Physics, the University of Tokyo, Japan. English language editing was performed by Editage (www.editage.com). Figures illustrating crystal structures were drawn using the Visualisation for Electronic Structural Analysis (VESTA) software (National Institute for Materials Science, Tsukuba, Japan)[54].

This work was partially supported by Grants-in-Aid for Scientific Research (grant numbers 19H05815, 19K15657, 20H02436, 21H01625, 21J14422, and 21K14715) from the Ministry of Education, Culture, Sports, Science, and Technology (MEXT), Japan; a CREST grant from the Japan Science and Technology Agency, Japan (grant number JPMJCR21O6); the Data Creation and Utilization-Type Material Research and Development Project (grant number JPMXP1122712807) from MEXT, Takahashi Industrial and Economic Research Foundation; The Naito Science & Engineering Foundation; and the Fujikura Foundation.

References

1 B. Dunn, H. Kamath and J.-M. Tarascon, *Science*, 2011, **334**, 928–935.

2 J. Janek and W. G. Zeier, *Nat. Energy*, 2016, 1, 16141.

3 J. Li, C. Ma, M. Chi, C. Liang and N. J. Dudney, *Adv. Energy Mater.*, 2015, **5**, 1401408.

4 Z. Gao, H. Sun, L. Fu, F. Ye, Y. Zhang, W. Luo and Y. Huang, *Adv. Mater.*, 2018, **30**, 1705702.

5 J. B. Goodenough and Y. Kim, *Chem. Mater.*, 2010, **22**, 587–603.

6 R. Fang, S. Zhao, Z. Sun, D. W. Wang, H. M. Cheng and F. Li, *Adv. Mater.*, 2017, **29**, 1606823.

7 N. Tanibata, H. Tsukasaki, M. Deguchi, S. Mori, A. Hayashi and M. Tatsumisago, *J. Mater. Chem. A Mater.*, 2017, **5**, 11224–11228.

8 C. Wang, J. Liang, Y. Zhao, M. Zheng, X. Li and X. Sun, *Energy Environ. Sci.*, 2021, **14**, 2577–2619.

9 K. Wang, Z. Gu, Z. Xi, L. Hu and C. Ma, *Nat. Commun.*, 2023, **14**, 1–10.

10 N. Tanibata, S. Takimoto, S. Aizu, H. Takeda and M. Nakayama, *J. Mater. Chem. A Mater.*, 2022, **10**, 20756–20760.

11 K. Xu, *Chem. Rev.*, 2004, **104**, 4303–4418.

12 D. Lin, Y. Liu and Y. Cui, *Nat. Nanotechnol.*, 2017, **12**, 194–206.

13 C. Yu, S. Ganapathy, E. R. H. V. Eck, H. Wang, S. Basak, Z. Li and M. Wagemaker, *Nat. Commun.*, 2017, **8**, 1086.

14 N. Ohta, K. Takada, L. Zhang, R. Ma, M. Osada and T. Sasaki, *Adv. Mater.*, 2006, **18**, 2226–2229.

15 Y. Li, W. Zhou, X. Chen, X. Lü, Z. Cui, S. Xin, L. Xue, Q. Jia and J. B. Goodenough, *Proc. Natl. Acad. Sci U S A*, 2016, **113**, 13313–13317.

16 S. Lou, F. Zhang, C. Fu, M. Chen, Y. Ma, G. Yin and J. Wang, *Adv. Mater.*, 2021, **33**, 2000721.

17 X. Yu and A. Manthiram, *Energy Environ. Sci.*, 2018, **11**, 527–543.

18 V. Thangadurai, S. Narayanan and D. Pinzaru, Chem. Soc. Rev., 2014, **43**, 4714.

19 J. van den Broek, S. Afyon and J. L. M. Rupp, *Adv. Energy Mater.*, 2016, **6**, 1600736.

20 S.-W. Baek, J.-M. Lee, T. Y. Kim, M.-S. Song and Y. Park, *J. Power Sources*, 2014, **249**, 197–206.

21 S. Chen, L. Nie, X. Hu, Y. Zhang, Y. Zhang, Y. Yu and W. Liu, *Adv. Mater.*, 2022, **34**, 2200430.

22 S. Wang, Y. Zhang, X. Zhang, T. Liu, Y.-H. Lin, Y. Shen, L. Li and C.-W. Nan, *ACS Appl. Mater. Interfaces*, 2018, **10**, 42279–42285.

23 K. Park, B. C. Yu, J. W. Jung, Y. Li, W. Zhou, H. Gao, S. Son and J. B. Goodenough, *Chem. Mater.*, 2016, **28**, 8051–8059.

24 X. Li, J. Liang, X. Yang, K. R. Adair, C. Wang, F. Zhao and X. Sun, *Energy Environ. Sci.*, 2020, **13**, 1429–1461.

25 S. Deng, M. Jiang, A. Rao, X. Lin, K. Doyle-Davis, J. Liang, C. Yu, R. Li, S. Zhao, L. Zhang, H. Huang, J. Wang, C. V. V. C. V. V. Singh, X. Sun, S. Deng, X. Lin, K. Doyle-Davis, J. Liang, C. Yu, R. Li, X. Sun, M. Jiang, A. Rao, C. V. V. C. V. V. Singh, S. Zhao, L. Zhang, J. Wang and H. Huang, *Adv. Funct. Mater.*, 2022, **32**, 2200767.

26 L. Zhou, T. T. T. Zuo, C. Y. Y. Kwok, S. Y. Y. Kim, A. Assoud, Q. Zhang, J. Janek and L. F. F. Nazar, *Nat. Energy*, 2022, **7**, 83–93.

27 C. Wang, S. Wang, X. Liu, Y. Wu, R. Yu, H. Duan, J. T. Kim, H. Huang, J. Wang, Y. Mo and X. Sun, *Energy Environ. Sci.*, 2023, **16**, 5136–5143.

28 A. M. Nolan, Y. Zhu, X. He, Q. Bai and Y. Mo, *Joule*, 2018, **2**, 2016–2046.

29 L. Kahle, A. Marcolongo and N. Marzari, *Energy Environ. Sci.*, 2020, **13**, 928–948.

30 R. Jalem, M. Nakayama and T. Kasuga, *J. Mater. Chem. A Mater.*, 2013, **2**, 720–734.

31 N. Tanibata, Y. Kondo, S. Yamada, M. Maeda, H. Takeda, M. Nakayama, T. Asaka, A. Kitajou and S. Okada, *Sci. Rep.*, 2018, **8**, 17199.

32 A. Sakuda, A. Hayashi and M. Tatsumisago, *Sci. Rep.* 2013 **3**, 1–5.

33 S. Choi, M. Jeon, W. D. Jung, S. Yang, S. Park, H. Il Ji, J. H. Lee, B. K. Kim, B. I. Sang and H. Kim, *Solid State Ion*, 2020, **346**, 115217.

34 L. Gao, F. Zhong, Y. Tong, S. Zhang, J. You, H. Wei, X. Yu, S. Xu and G. Zhao, *ACS Appl. Energy Mater.* , DOI:10.1021/ACSAEM.2C01343/ASSET/IMAGES/LARGE/AE2C01343_0005.JPEG.

35 J.-S. Kim, Y. J. Kim, D. Han, K.-W. Nam, G. Kwon, T. W. Heo, H.-G. Jung, K. J. Yoon and H. Kim, *J. Mater. Chem. A Mater.*, 2023, **11**, 7457–7467.

36 B. Bhushan and M. Nosonovsky, *Acta Mater.*, 2003, **51**, 4331–4345.

37 Elasticity - Materials Project Documentation.

38 A. Jain, S. P. Ong, G. Hautier, W. Chen, W. D. Richards, S. Dacek, S. Cholia, D. Gunter, D. Skinner, G. Ceder and K. A. Persson, *APL Mater.*, 2013, 1, 011002.

39 S. Aizu, S. Takimoto, N. Tanibata, H. Takeda, M. Nakayama and R. Kobayashi, *J. Am. Ceram. Soc.*, 2023, **106**, 3035–3044.

40 N. Tanibata, M. Kato, S. Takimoto, H. Takeda, M. Nakayama and H. Sumi, *Adv. Energy Sustain. Res.*, 2020, **1**, 2000025.

41 N. Tanibata, S. Takimoto, K. Nakano, H. Takeda, M. Nakayama and H. Sumi, *ACS Mater. Lett.*, 2020, **2**, 880–886.

42 K. Choudhary, M. Bercx, J. Jiang, R. Pachter, D. Lamoen and F. Tavazza, *Chem. Mater.*, 2019, **31**, 5900–5908.

43 R. Kobayashi, *J. Open Source Softw.*, 2021, **6**, 2768.

44 R. Hill, *Proc. Phys. Soc.*, 1952, **65**, 349–354.

45 X. S. Yang and S. Deb, *Neural Comput. Appl.*, 2014, 24, 169–174.

46 S. Aizu, S. Takimoto, N. Tanibata, H. Takeda, M. Nakayama and R. Kobayashi, *J. Am. Ceram. Soc.*, 2023, **106**, 3035–3044.

47 J. Maier, *J. Am. Ceram. Soc.*, 1993, **76**, 1228–1232.

48 A. Van der Ven, G. Ceder, M. Asta and P. D. Tepesch, *Phys. Rev. B*, 2001, **64**, 184307.

49 H. Schichlein, A. C. Müller, M. Voigts, A. Krügel and E. Ivers-Tiffée, *J. Appl. Electrochem.*, 2002, **32**, 875–882.

50 H. Sumi, H. Shimada, Y. Yamaguchi, T. Yamaguchi and Y. Fujishiro, *Electrochim. Acta*, 2020, **339**, 135913.

51 J. T. S. Irvine, D. C. Sinclair and A. R. West, *Adv. Mater.*, 1990, **2**, 132–138.

52 N. C. Halder and C. N. J. Wagner, *Acta Crystallogr.*, 1966, **20**, 312–313.

53 S. Ohta, S. Komagata, J. Seki, T. Saeki, S. Morishita and T. Asaoka, *J. Power Sources*, 2013, **238**, 53–56.

54 K. Momma and F. Izumi, *J. Appl. Crystallogr.*, 2008, **41**, 653–658.

ARTICLE

Data Availability

All relevant data are available from the

corresponding author on reasonable request.